

**Relativistic flying forcibly oscillating reflective diffraction grating**

Jie Mu,<sup>1</sup> Timur Zh. Esirkepov<sup>2,\*</sup>, Petr Valenta<sup>1,3</sup>, Yanjun Gu,<sup>1</sup> Tae Moon Jeong<sup>1</sup>, Alexander S. Pirozhkov<sup>2</sup>,  
James K. Koga<sup>2</sup>, Masaki Kando<sup>2</sup>, Georg Korn,<sup>1</sup> and Sergei V. Bulanov<sup>1,2</sup>

<sup>1</sup>*ELI Beamlines Project, Institute of Physics of the ASCR, Na Slovance 2, 18221 Prague, Czech Republic*

<sup>2</sup>*Kansai Photon Science Institute, National Institutes for Quantum and Radiological Science and Technology, 8-1-7 Umemidai, Kizugawa, Kyoto 619-0215, Japan*

<sup>3</sup>*Faculty of Nuclear Sciences and Physical Engineering, Czech Technical University in Prague, Brehova 7, 11519 Prague, Czech Republic*



(Received 30 June 2020; accepted 8 October 2020; published 2 November 2020)

Relativistic flying forcibly oscillating reflective diffraction gratings are formed by an intense laser pulse (driver) in plasma. The mirror surface is an electron density singularity near the joining area of the wake wave cavity and the bow wave; it moves together with the driver laser pulse and undergoes forced oscillations induced by the field. A counterpropagating weak laser pulse (source) is incident at grazing angles, being efficiently reflected and enriched by harmonics. The reflected spectrum consists of the source pulse base frequency and its harmonics, multiplied by a large factor due to the double Doppler effect.

DOI: [10.1103/PhysRevE.102.053202](https://doi.org/10.1103/PhysRevE.102.053202)

**I. INTRODUCTION**

Bright sources of electromagnetic radiation with the spectral range from extreme ultraviolet to x rays have attracted a great deal of attention because of their great potential for both fundamental science and practical applications (e.g., in biology, medicine, and materials science) [1,2]. One of the ways toward developing ultrashort intense electromagnetic pulse sources is a simultaneous frequency upshift and pulse compression. This occurs in the reflection of an electromagnetic wave from a fast approaching mirror, which is a manifestation of the double Doppler effect. According to the Einstein prediction [3], in the head-on wave-mirror collision, the reflected electromagnetic pulse is compressed and its frequency is upshifted by the same factor  $(c + v_M)/(c - v_M) \approx 4\gamma_M^2$ , where  $v_M$  is the mirror velocity,  $c$  is the speed of light in vacuum, and  $\gamma_M = (1 - v_M^2/c^2)^{-1/2}$  is the mirror Lorentz factor.

There are a few physical realizations of this concept. Perhaps the earliest are the electromagnetic wave reflection at a moving relativistic electron slab [4] and at moving ionization fronts [5–7].

A potentially high repetition generation of frequency-upshifted high-intensity quasimonochromatic electromagnetic pulses [8–11] uses a laser-driven breaking wake wave in underdense plasma as the relativistic flying mirrors (RFMs) which reflect, compress, and focus a counterpropagating laser pulse (for details see the reviews in [12,13] and references therein). An increase of the intensity of counterpropagating laser pulses modifies this scheme, adding generation of high-order harmonics at the mirror [14]; the spectrum of the reflected light consists of harmonics of the incident pulse base frequency, all multiplied by approximately  $4\gamma_M^2$ .

The flying mirror can be a laser-accelerated thin electron layer ejected by an intense laser pulse from a thin foil [15]. An ensemble of flying mirrors producing high-intensity attosecond pulses is realized by electron layers consequently ejected at every period of the intense incident laser [16]. Due to multiple reflections on many semitransparent electron layers, the conversion efficiency can be as high as  $4\gamma_M^2 \gg 1$ , where energy is gained via the momentum transfer from the flying electron layers to the reflected radiation [16].

The relativistic oscillating mirrors (ROMs) are formed at the surface of an overdense plasma, when a strong laser field both induces the nonlinearly oscillating electron density modulations and gets reflected off them, producing high-order harmonics [17–19]. When a dense plasma slab is accelerated by a high-contrast ultraintense laser pulse in the regime of radiation pressure dominant acceleration, it gains energy as a receding mirror and acts as an approaching mirror for a counterpropagating intense laser pulse [20]; in addition, it acts as a relativistic oscillating mirror in the comoving reference frame so that the reflected radiation contains high-order harmonics, upshifted due to the double Doppler effect.

Here we present a physical realization of the relativistic mirror, the relativistic flying forcibly oscillating mirror (RFFOM). It appears as a surface of high electron density corresponding to a folding singularity created by an intense laser pulse propagating in plasma. Being modulated by the laser field, this surface acts as a reflective diffraction grating for a counterpropagating electromagnetic wave.

The paper is organized as follows. In Sec. II the mechanism of the RFFOM concept is introduced. Section III gives a simplified theory based on the assumption of an inclined ideal flat mirror. Section IV introduces the simulation setup and the basic parameters. In Secs. V and VI we analyze the properties of the reflected wave and its spectrum using a three-dimensional (3D) simulation and high-resolution 2D simulations, respectively. In Sec. VII the influence of thermal

\*timur.esirkepov@qst.go.jp

effects on the RFFOM is investigated. Section VIII summarizes the results and discusses possible applications of the concept.

## II. RFFOM MECHANISM

An intense laser pulse propagating in underdense plasma excites wake waves [21–23]. The laser field pushes electrons not only along the laser axis, but also aside, creating a cavity void of electrons. Depending on the relation between the kinetic energy of transversely pushed electrons  $\mathcal{E}_{e\perp}$  and the electrostatic potential of the cavity  $\varphi$ , one can see three patterns of the first wake wave period. When  $\mathcal{E}_{e\perp} \ll e\varphi$ , the cavity rear has a smooth surface, which can be used as a RFM [8]. Here  $e$  is the electron charge. For  $\mathcal{E}_{e\perp} \gtrsim e\varphi$ , electrons forming the cavity wall overshoot the axis at the cavity rear, which causes the transverse wave breaking [24], playing an important role in the electron injection into the acceleration phase of the wake wave. A tightly focused laser pulse can push electrons so that  $\mathcal{E}_{e\perp} \gg e\varphi$  and electrons form a bow wave [25], which detaches from the cavity wall in the head of the laser pulse. A propagation of transversely pushed electrons through unperturbed electrons is a multistream flow. In the approximation of a continuous electron fluid, such flows have density singularities whose existence, universality, and structural stability are explained by catastrophe theory [26]. The fold singularity corresponds to the electron density jumps at the cavity wall and bow wave boundary. At their joining, the electron density is even higher and corresponds to the cusp singularity. The fold singularity is indeed a fold of the phase distribution of initially unperturbed electrons, projected into a space to form the density distribution [27–29].

The cusp and the adjacent folds act as a pair of mirrors joined at some angle (cusped mirror), which undergoes forced oscillations induced by the laser field (Fig. 1). It partially reflects a counterpropagating electromagnetic wave (source). The reflected radiation is enriched by high-order harmonics, because the cusped mirror is oscillating, like ROMs [17], and all of the reflected spectrum is upshifted because the cusped mirror moves with a high speed, like RFMs [8]. Moreover, the source can have a grazing incidence on the mirror surfaces, because at the point of the bow wave detachment from the cavity wall, the surfaces of the highest electron density can make a relatively small angle with respect to the laser axis. These angles can be controlled by the laser focal spot size and initial plasma density, in accordance with the condition of the bow wave formation [25]. As is known, the smaller the grazing incidence angle, the higher the reflection efficiency. In our case, however, the increase of the reflection efficiency is accompanied by a decrease of the frequency upshift factors.

The cusped mirror is a RFFOM, combining the properties of a RFM and a ROM. The surface of the cusped mirror is periodically modulated by the laser field; therefore, the cusped mirror has the properties of a reflective diffraction grating.

A source laser pulse is reflected from the cusped mirror; high-order harmonics are generated due to the mirror oscillations as in ROMs and the whole reflected spectrum is upshifted as in RFMs. The reflected radiation goes at discrete angles corresponding to the diffraction orders of a relativistic flying reflective diffraction grating. The feasibility of the

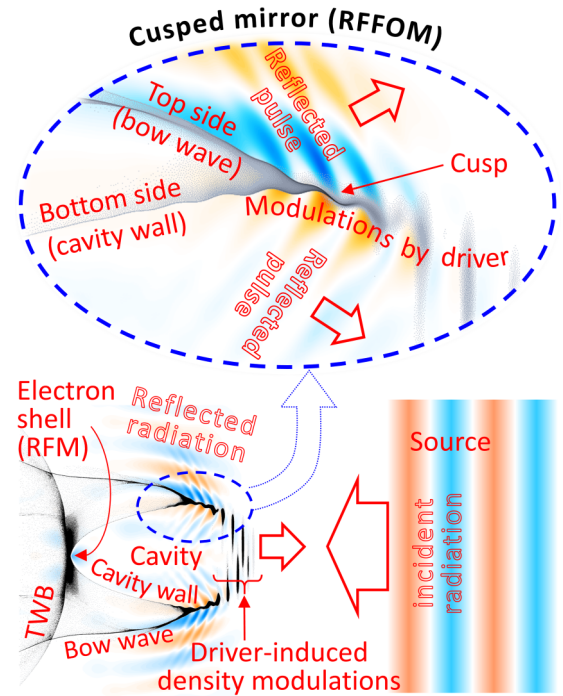


FIG. 1. The RFFOM scheme. On the bottom the driver pulse (not shown but revealed via density modulations) creates a cavity and bow wave in underdense plasma (2D PIC simulation of Sec. VI). Overshooting electrons cause transverse wave breaking (TWB). Shown on top is a close-up of the area near the cusp. A counterpropagating source pulse is reflected off the sides of the cusped mirror, forcibly oscillating under the action of the driver. The blue-red color scale is for the electric field and grayscale is for the electron density.

above-described RFFOM is demonstrated using 2D and 3D particle-in-cell (PIC) simulations.

We note that the cusp and the portions of adjacent folds have their own self-emission [27–30] when only the driver pulse is present. In particular, the cusp emits high-frequency electromagnetic radiation in a cone around the vector of the average velocity of the cusp. The constructive interference is gained only for wavelengths which are emitted by the regions having size shorter than the wavelength in the radiation propagation direction. This condition is always satisfied for the cusp singularity. In analogy with the moving oscillating charge, the cusp emits the high-order harmonics observed in experiments [27–29]. Here we do not consider this self-emission. In the simulations shown below, the source pulse and consequently the reflected pulse have different polarization with respect to the driver and the reflected radiation disappears in the absence of the source.

## III. MODEL

In order to analyze the base frequency and direction angle of electromagnetic radiation reflected from the cusped mirror, we use a simplified model, neglecting oscillations of the mirror surface (Fig. 2). We consider a moving ideal flat mirror in a 2D space  $(x, y)$ , where the mirror velocity vector is  $\{\beta c, 0\}$ , with  $\beta = v_M/c$ . The mirror is inclined with respect to its velocity; the normal vector to its surface

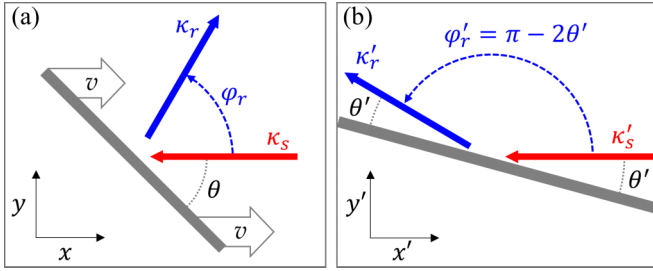


FIG. 2. Positional relationship of the moving inclined mirror, and incident and reflected waves in the (a) laboratory and (b) comoving reference frames.

is  $\{\sin \theta, \cos \theta\}$ . A counterpropagating electromagnetic wave with frequency  $\omega_s$  is incident on the mirror; its wave number vector is  $\kappa_s = \{-\omega_s/c, 0\}$ . The reflected electromagnetic wave has a frequency of  $\omega_r$  and a wave number vector of  $\kappa_r = (\omega_r/c)\{\cos \phi_r, \sin \phi_r\}$ .

The parameters of the reflected wave are obtained by changing to the reference frame of the mirror, considering specular reflection, and changing back to the laboratory reference frame

$$\omega_r = \omega_s \frac{1 + \beta}{1 - \beta \cos \phi_r}, \quad (1)$$

$$\cos \phi_r = \frac{(1 + \beta)^2 \tan^2(\theta) - 1}{(1 + \beta)^2 \tan^2(\theta) + 1}. \quad (2)$$

For large values of  $\gamma = (1 - \beta^2)^{-1/2} \rightarrow \infty$  and fixed angle  $0 \leq \theta \leq \pi/2$ , we have

$$\omega_r = \omega_s \frac{5 - 3 \cos 2\theta}{1 + \cos 2\theta} - O\left(\frac{1}{\gamma^2}\right), \quad (3)$$

$$\cos \phi_r = \frac{3 - 5 \cos 2\theta}{5 - 3 \cos 2\theta} + O\left(\frac{1}{\gamma^2}\right). \quad (4)$$

We note that the expansion of Eq. (3) diverges for  $\theta \rightarrow \pi/2$  (i.e., for near-normal incidence). Nevertheless, the larger the  $\gamma$ , the greater the well-approximated threshold for  $\theta$ ; for example, for  $\gamma = 10$ , the approximation is good for  $0 \leq \theta \leq \pi/4$  with the maximum (overestimation) error of 2%. In Eq. (4) the expansion is valid for the whole interval of  $0 \leq \theta \leq \pi/2$ ; for example, for  $\gamma = 10$ , the maximum (overestimation) error is 0.25%. In the limit of the glancing angle  $\theta \rightarrow 0$ , reflection does not occur:  $\omega_r \rightarrow \omega_s$  and  $\cos \phi_r = -1$ .

According to Eqs. (3) and (4), for large  $\gamma$ , the mirror inclined at  $\theta = \arccos(\frac{3}{5})/2 \approx 26.6^\circ$  reflects radiation at  $90^\circ$  with frequency  $\omega_r \approx 2\omega_s$ . If the driver pulse is sufficiently intense and tightly focused (e.g., due to relativistic self-focusing), the transversely pushed electrons move with relativistic velocity. Since the driver velocity is also relativistic, the bow wave outer boundary makes an angle of  $\theta \approx 45^\circ$  with the laser axis [25]. In this case, from the expansions in Eqs. (3) and (4) we obtain  $\omega_r \approx 5\omega_s$  and  $\phi_r \approx \arccos(\frac{3}{5}) \approx 53^\circ$ , independent of the mirror velocity for sufficiently large  $\gamma$ .

Equation (1) represents an ellipse in polar coordinates  $(\omega_s, \phi_r)$  [9]. In the coordinates  $(k_x, k_y)$ , which are the components of the reflected wave number vector  $\kappa_r = \{k_x, k_y\}$ , we have  $\omega_r = c(k_x^2 + k_y^2)^{1/2}$  and  $\phi_r = \arctan(k_y/k_x)$ , so the

leftmost focus of the ellipse is at  $(0,0)$  and the major axis coincides with the  $x$  axis; the leftmost point of the ellipse is  $\omega_r|_{\phi_r=\pi} = \omega_s$ , which means transmitted radiation; the rightmost point of the ellipse is  $\omega_r|_{\phi_r=0} = \omega_s(1 + \beta)/(1 - \beta) \approx 4\gamma^2\omega_s$ , which means exactly backward reflection. If there exist harmonics of the base frequency, each harmonic order sits on its own ellipse with the same leftmost focus.

If the source pulse has sufficiently low frequency, its wavelength inside the plasma is significantly longer than in vacuum,  $\tilde{\lambda}_s = \lambda_s(1 - \omega_{pe}^2/\omega_s^2)^{-1/2}$ , where  $\omega_{pe} = \sqrt{4\pi e^2 n_e/m_e}$  is the Langmuir frequency. Here  $n_e$  is the electron density and  $m_e$  is the electron mass. In this situation, Eq. (1) becomes [12]

$$\omega_r = \frac{\psi_s + \beta \cos(\phi_r) \sqrt{\psi_s^2 - \omega_{pe}^2(1 - \beta^2 \cos^2 \phi_r)}}{1 - \beta^2 \cos^2 \phi_r}, \quad (5)$$

$$\psi_s = \omega_s + \beta \sqrt{\omega_s^2 - \omega_{pe}^2} \quad (6)$$

and the reflection angle is determined by the relation

$$\frac{\sin \phi_r}{\cos(\phi_r) - \beta \beta_{s,ph}} = \frac{2\gamma^2 \tan \theta}{\tan^2(\theta) - \gamma^2}, \quad (7)$$

where  $\beta_{s,ph} = v_{s,ph}/c > 1$  is the normalized phase velocity of the source pulse,

$$\begin{aligned} \beta_{s,ph} &= \omega_r / \sqrt{\omega_r^2 - \omega_{pe}^2} \\ &= \frac{\psi_s + \beta \cos(\phi_r) \sqrt{\psi_s^2 - \omega_{pe}^2(1 - \beta^2 \cos^2 \phi_r)}}{\psi_s \beta \cos(\phi_r) + \sqrt{\psi_s^2 - \omega_{pe}^2(1 - \beta^2 \cos^2 \phi_r)}}. \end{aligned} \quad (8)$$

In the limit  $\omega_{pe} \rightarrow 0$  and  $\psi_s \rightarrow (1 + \beta)\omega_s$ , Eq. (5) reduces to Eq. (1). According to Eq. (5), the maximum frequency upshift (at  $\phi_r = 0$ ) in plasma is slightly less than that in vacuum,

$$\begin{aligned} \omega_r|_{\phi_r=0} &= \gamma^2(\psi_s + \beta \sqrt{\psi_s^2 - \omega_{pe}^2/\gamma^2}) \\ &< \gamma^2(1 + \beta)\psi_s. \end{aligned} \quad (9)$$

#### IV. SIMULATION SETUP

To study the laser plasma interaction under the conditions when the bow wave is formed, we carry out 2D and 3D PIC simulations using the EPOCH code [31] and REMP code [32]. The plasma is fully ionized and homogeneous. The ion response is neglected due to a large ion-to-electron mass ratio, relatively low electron density, and a short time of the considered interaction. The electron density is  $n_e = 1.14 \times 10^{19} \text{ cm}^{-3} \times (1 \mu\text{m}/\lambda_d)^2 = 0.01n_c$ , where  $n_c = \pi/r_e \lambda_d^2 = 1.115 \times 10^{21} \text{ cm}^{-3} \times (1 \mu\text{m}/\lambda_d)^2$  is the critical density,  $r_e = e^2/m_e c^2$  is the classical electron radius, and  $\lambda_d = 2\pi c/\omega_d$  is the wavelength, with  $\omega_d$  the frequency of the driver laser and  $c$  the speed of light in vacuum.

The driver laser pulse is linearly polarized with its electric field vector along the  $y$  axis and its dimensionless amplitude is  $a_d = eE_d/m_e \omega_d c = 6.62$ , corresponding to an intensity of  $I_d = 6 \times 10^{19} \times (1 \mu\text{m}/\lambda_d)^2 \text{ W/cm}^2$ , where  $E_d$  is the maximum electric field of the driver. Its full width at half maximum is  $5\lambda_d \times 5\lambda_d$  (along the  $x$  and  $y$  axes) in 2D simulations and  $10\lambda_d \times 4\lambda_d \times 4\lambda_d$  (along the  $x$ ,  $y$ , and  $z$  axes) in the 3D

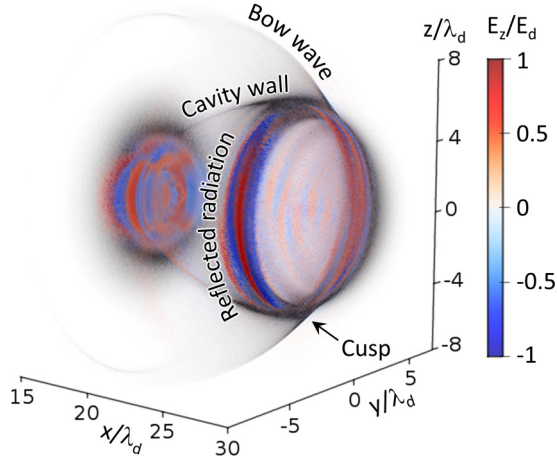


FIG. 3. Wake wave cavity, bow wave, and cusp seen in the electron density distribution (in grayscale). The reflected electric field normalized to that of the driver  $E_d$  is shown by the blue-red color scale.

simulation. The driver focus is at the left boundary of the simulation box. In the 3D simulation, the transverse sizes of the driver and source laser pulses are less than in 2D simulations due to the limited computational resources.

The source laser pulse has perpendicular polarization; its electric field vector is along the  $z$  axis. This helps to distinguish the driver, the source, and the reflected radiation, as was done in previous publications [8]. Moreover, it helps to distinguish the reflected signal from the cusp self-emission. The source has a longer wavelength  $\lambda_s = 8\lambda_d$ . This helps to more easily resolve and analyze the strongly upshifted reflected radiation enriched with high-order harmonics with limited computing resources. The source pulse dimensionless amplitude is  $a_s = 0.05$ , corresponding to an intensity of  $I_s = 5.35 \times 10^{13} \text{ W/cm}^2$ . It is sufficiently weak in order not to affect the motion and structure of the cusped mirror [33]. Its full width at half maximum is  $8\lambda_d \times 20\lambda_d$  in 2D simulations and  $8\lambda_d \times 10\lambda_d \times 10\lambda_d$  in the 3D simulation. Its transverse size is large enough to see reflection from bow waves.

The simulation results are shown in Figs. 7(a), where Figs. 3 and 4 represent 3D simulation while Figs. 5–9 show 2D simulations with similar parameters. In the following  $T_d = \lambda_d/c$  is the period of the driver laser cycle.

### V. 3D SIMULATION

An excitation of the wake wave and bow wave by the driver pulse, the formation of the cavity, and the reflection of the source pulse from the cusped mirror can be seen in the 3D PIC simulation (Fig. 3). Here the simulation box has a size of  $30\lambda_d \times 30\lambda_d \times 30\lambda_d$ . The spatial grid mesh is  $\Delta x/\lambda_d = \frac{1}{30}$ ,  $\Delta y/\lambda_d = \frac{1}{30}$ , and  $\Delta z/\lambda_d = \frac{1}{30}$ . Plasma uniformly fills the cube with coordinates of  $0\lambda_d \leq x \leq 30\lambda_d$ ,  $-15\lambda_d \leq y \leq 15\lambda_d$ , and  $-15\lambda_d \leq z \leq 15\lambda_d$ . The total number of quasiparticles is  $5.7 \times 10^8$ .

The reflected radiation in Fig. 3 is computed as follows. First, the difference is taken between the electromagnetic fields in two separate simulations, one with the source pulse and another without it. The electromagnetic field obtained in

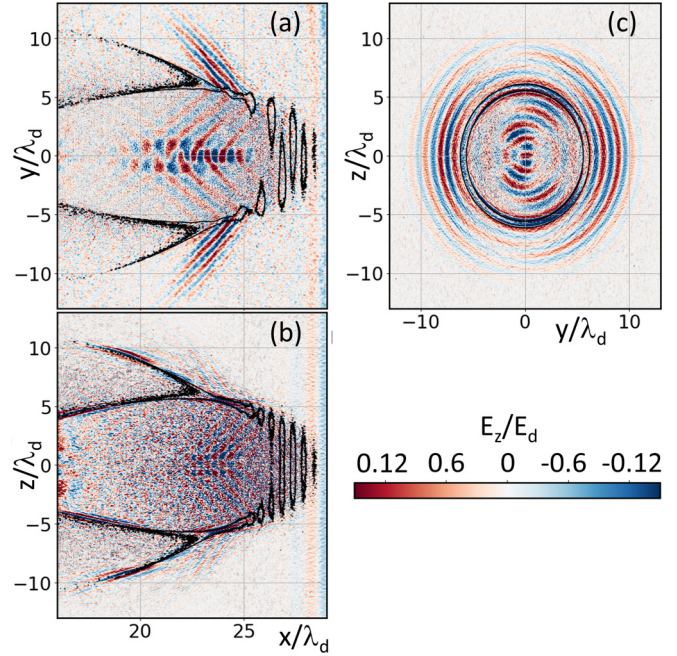


FIG. 4. Cross sections of the box shown in Fig. 3 along the planes (a)  $(x, y, z = 0)$ , (b)  $(x, y = 0, z)$ , and (c)  $(x = 22.5, y, z)$ . The blue-red color scale for the electric field normalized to that of the driver  $E_d$  contours for electron density.

this way represents the incident source pulse together with the reflected radiation [10]. Second, the low-frequency component is filtered out, thus the field representing the source pulse is removed so that the remaining component corresponds to the reflected radiation.

As can be seen in Figs. 3 and 4(a), reflection occurs in the regions of high electron density. Reflection starts at the cusp, a location where the cavity wall joins the outline of the bow wave. Then it happens at the rear of the cavity. The latter is a realization of the RFM by the breaking wake wave, as described in Ref. [8].

Here we focus on the reflection at the cusp. As can be seen in Figs. 4(a) and 4(c), the reflected radiation goes at some angle off axis, from both sides of the cusped mirror near the cusp, in the form of two short-wavelength pulses: An outer pulse initially goes outside the cavity and an inner pulse initially goes inside the cavity. As expected, the reflected radiation wavefronts correspond to a conical mirror; in particular, the cross section in the plane of the driver axis and polarization demonstrates a nearly flat wave front cross section [Fig. 4(a)], in agreement with the model assumption in Sec. III. These fronts certainly become almost spherical when the reflected pulses propagate at a distance much greater than their width.

The frequency upshift of the reflected radiation is obvious: The reflected pulse wavelength is significantly shorter than the electron density modulation induced by the driver, which in turn is much shorter than the source pulse wavelength ( $\omega_s = \omega_d/8$ ). We note that the outer pulse has a shorter wavelength than the inner pulse, in accordance with their propagation direction, which corresponds to reflection from different sides of

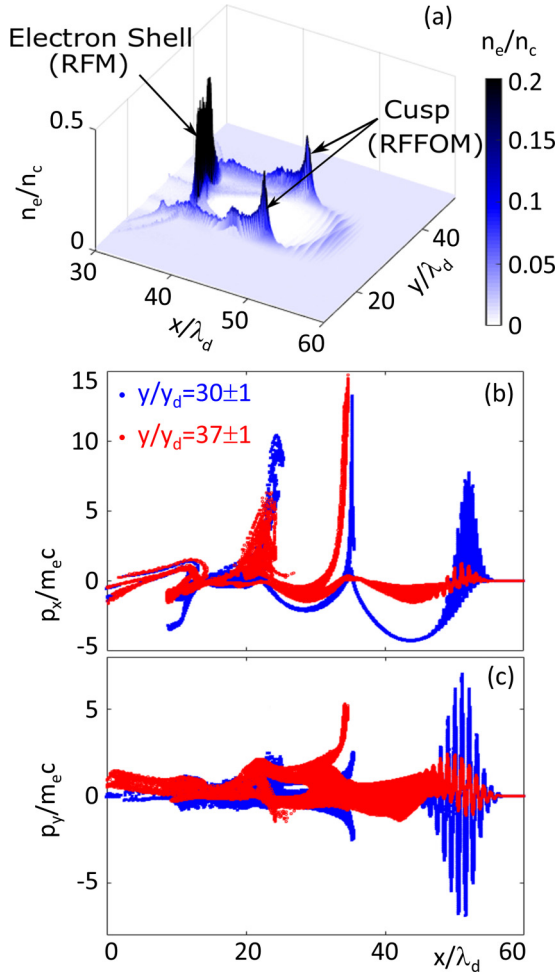


FIG. 5. (a) Electron density distribution in the  $(x, y)$  plane at  $t = 54T_d$ . (b) Longitudinal  $p_x$  and (c) transverse  $p_y$  electron momenta vs the  $x$  coordinate, for electrons in the strip near the axis  $29\lambda_d \leq y \leq 31\lambda_d$  (blue) and in the strip containing the cusp  $36\lambda_d \leq y \leq 38\lambda_d$  (red).

the cusped mirror with different inclination angle with respect to the driver axis.

Near the cusp, the electron density is comparable to that at the cavity rear, at the breaking point of the wake wave. Both the cusped mirror and the electron shell at the cavity rear provide efficient reflection due to strong localization of electrons. In addition, grazing incidence enhances the cusped mirror reflectivity, although at the expense of the greater off-axis reflection angle and correspondingly the lower frequency upshift factor, as follows from the model in Sec. III.

## VI. HIGH-RESOLUTION 2D SIMULATIONS

In order to see the spectral properties of the reflected radiation, we performed 2D PIC simulations in the moving window with higher resolution, for a grid mesh size of  $\Delta x/\lambda_d = 1/1024$  and  $\Delta y/\lambda_d = 1/256$ . The conical cusped mirror seen in the 3D simulation appears in 2D simulation as two cusped mirrors [Fig. 5(a)], analogously to the cross section in Fig. 4(a). We note that the cusp maintains a stable structure for more than 150 driver laser cycles. The cusped

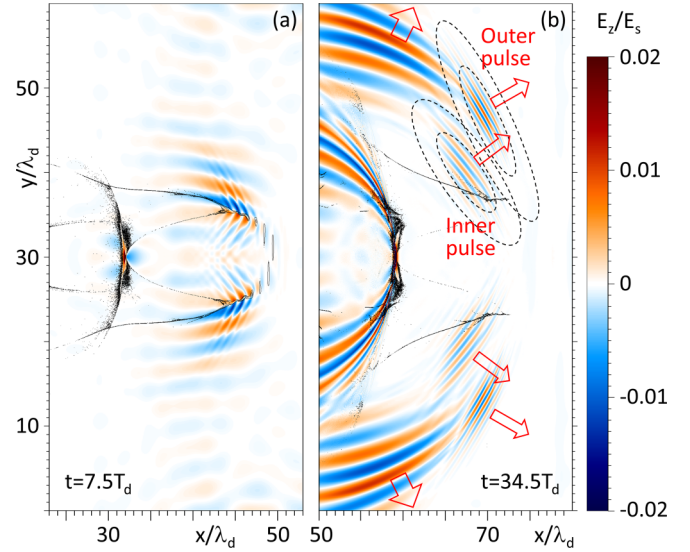


FIG. 6. Electric field  $E_z$  after the high-pass filter, for  $\omega \geq 2\omega_s$ , at (a)  $7.5T_d$  and (b)  $34.5T_d$ . The black thin curves correspond to electron densities of  $0.03n_c$ ,  $0.04n_c$ , and  $0.05n_c$ . Arrows show the propagation direction. Dashed ellipses show the reflected outer and inner pulses selected for spectrum analysis by the Gaussian spatial filters: The filter value is 0.999 for small ellipses and  $10^{-6}$  for larger ones.

mirror is a phase object; at each moment of time, it consists of different electrons, continuously flowing through it [29].

Figures 5(b) and 5(c) display the longitudinal  $p_x$  and transverse  $p_y$  momenta, respectively, for the electrons in different regions. The electrons located near the driver axis in a strip bounded as  $29\lambda_d \leq y \leq 31\lambda_d$  (shown in blue) demonstrate well-known patterns of the wake wave behind an intense short laser pulse. Characteristic modulations induced by the driver field indicate the location of the driver pulse. Longitudinal wave breaking is seen at  $x \approx 22\lambda_d$  and  $x \approx 35\lambda_d$  in Fig. 5(b); transverse wave breaking is seen at  $x \approx 33.5\lambda_d$  in Fig. 5(c).

The momentum distributions of electrons at the periphery, in the strip containing the cusp ( $36\lambda_d \leq y \leq 38\lambda_d$ ), are shown in red in Figs. 5(b) and 5(c). For electrons near the cusp, the longitudinal momentum  $p_x$  is negative [Fig. 5(b)], which means that these electrons move backward with respect to the  $x$  axis, in striking contrast to the motion of the cusp in the forward direction. The transverse momentum  $p_y$  of electrons near the cusp fills a relatively wide strip stretching from negative to positive values [Fig. 5(c)], which indicates a multistream flow.

Upon reflection from the cusped mirror, the source pulse transforms into several well-separated pulses with different wavelength and propagation direction, as seen in Fig. 6. Reflected pulses are almost bilaterally symmetric with respect to the  $x$  axis, which correlates with the approximate reflection symmetry of the cavity, bow waves, and cusps.

The pulses with the longest wavelength (the lowest frequency) are seemingly reflected from the outer side of the cusped mirror (farthest from the driver axis). They have a frequency multiplication factor of approximately 2.6 and propagate at an angle of approximately  $75^\circ$  with respect to the  $x$  axis, in accordance with the asymptotes in Eqs. (1) and (2).

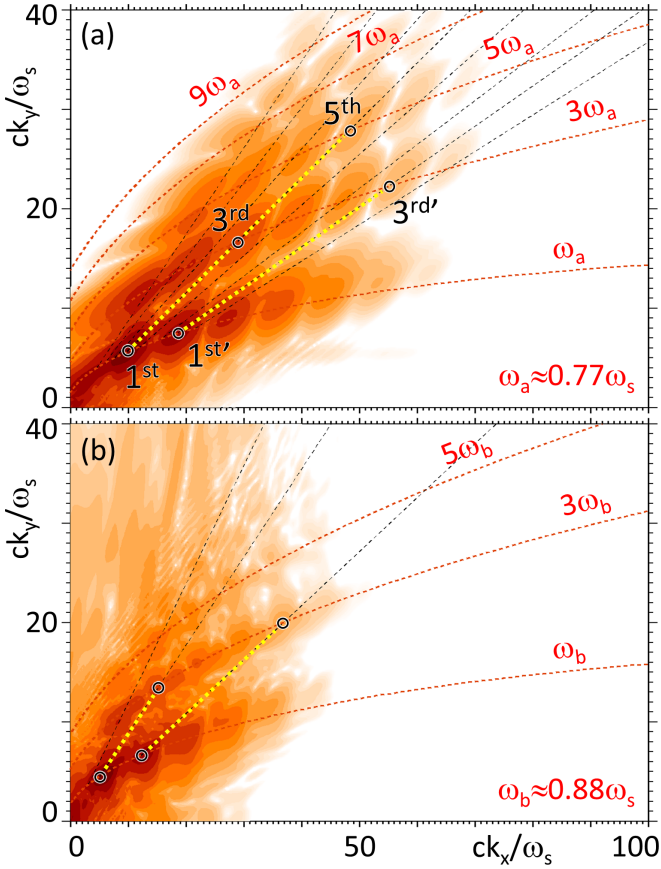


FIG. 7. Frequency spectrum of the (a) outer and (b) inner pulses selected by the Gaussian spatial filter shown in Fig. 6(b). Red dashed curves represent the frequency upshift dependence on the reflection angle  $\phi_r = \arctan(k_y/k_x)$  [Eq. (5)], where  $\omega_s$  is replaced by the odd harmonics of  $\omega_a$  and  $\omega_b$ . Radial black dotted lines are for (a)  $22^\circ \pm 1.8^\circ$ ,  $30^\circ \pm 3^\circ$ ,  $37^\circ$ , and  $41^\circ$  and (b)  $28.5^\circ$ ,  $41.5^\circ$ , and  $50^\circ$ . Black circles emphasize the peaks in the frequency spectrum corresponding to the harmonics and diffraction orders.

The pulses with the shorter wavelengths (higher frequencies) are reflected from both sides of the cusped mirror. The outer pulse propagates away from the  $x$  axis, while the inner pulse initially propagates toward the  $x$  axis. In the upper half plane in Fig. 6(b), the outer pulse originates from the top of the cusped mirror at  $y > 30\lambda_d$ , while the inner pulse originates from top of the cusped mirror at  $y < 30\lambda_d$ .

The strikingly different wavelength and propagation direction of the reflected well-separated pulses indicate that reflection occurs at a relativistic flying reflective diffraction grating. In addition to a specularly reflected wave, the grating diffracts the incident wave at different angles. Due to the Doppler effect, the frequency upshift factor is greater for smaller diffraction (reflection) angles, according to Eqs. (1) and (5).

The outer and inner pulses contain high-order harmonics due to oscillations of the reflecting facets of the cusped mirror imposed by the driver laser. Their spatial spectra are shown in Fig. 7. The spectra resemble an opened folding fan. The distribution of the electromagnetic energy density is discretized with respect to both the angle and the wave number

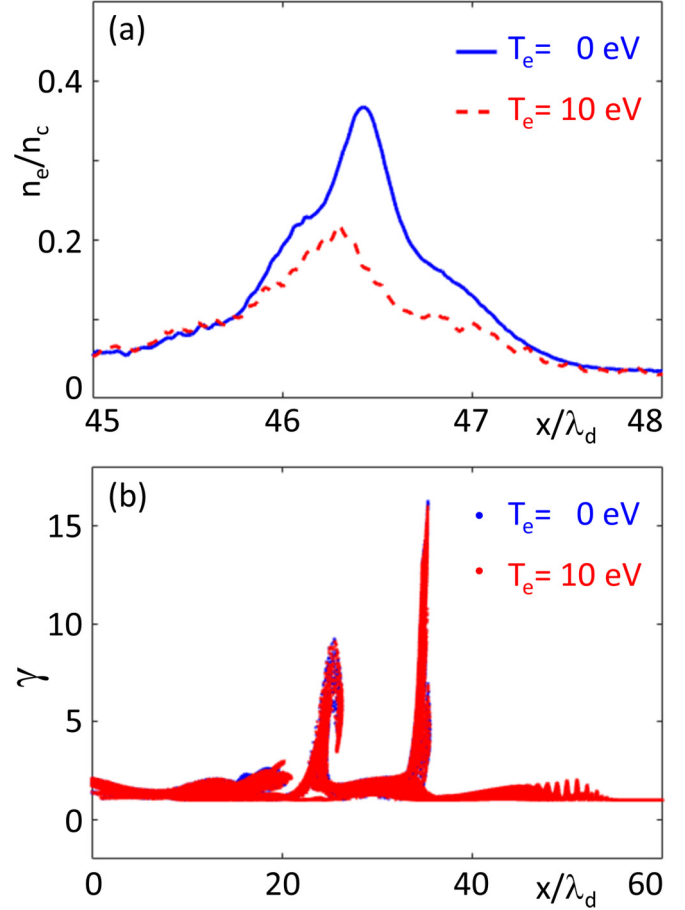


FIG. 8. (a) Cross section of the electron density near the cusp at  $y = 36.67\lambda_d$  and (b) the Lorentz factor  $\gamma$  of electrons near the cusp in the strip bounded as  $36 \leq y \leq 38\lambda_d$ , for two simulations with different initial electron temperature. The result for  $T_e = 0$  eV is marked in blue (hardly visible); the result for  $T_e = 10$  eV is marked in red.

(or frequency). The discretization with respect to the angle corresponds to the property of the cusped mirror to act as a reflective diffraction grating. The discretization with respect to the wave number (or frequency) reveals high-order harmonic generation due to the cusped mirror oscillations induced by the driver pulse. The well-separated hot spots in Fig. 7 represent diffraction orders along the angle and harmonic orders along the wave number (or frequency).

The cusped mirror moves with the velocity close to the group velocity of the driver pulse,  $\beta = \sqrt{1 - \omega_{pe}^2/\omega_d^2} \approx 0.995$ ; the corresponding Lorentz factor is  $\gamma = \omega_d/\omega_{pe} = 10$ . The source pulse has a relatively low frequency; therefore, its wavelength inside plasma is longer than in vacuum,  $\tilde{\lambda}_s \approx 1.67\lambda_s$ . According to Eq. (5), the frequency upshift factor for radiation reflected at  $30^\circ$  with respect to the driver pulse axis is  $\omega_r/\omega_s \approx 11.4$ . This is in good agreement with the position of the first harmonic (hot spot) emitted at the above-specified angle in Fig. 7(a). The hot spots are arranged along curves close to ellipses defined by Eq. (5). Each curve corresponds to an odd harmonic of somewhat downshifted frequency of the source pulse.

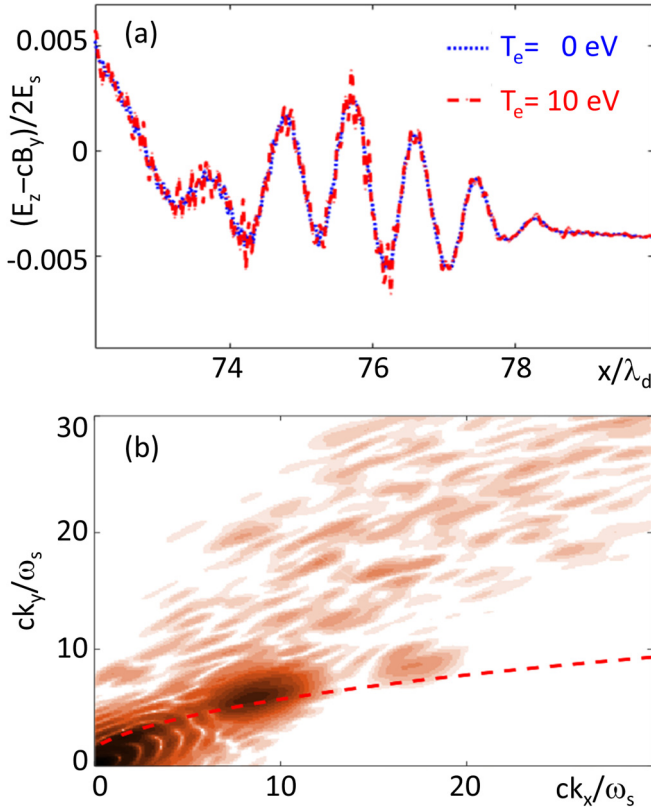


FIG. 9. (a) Combination of the electromagnetic field components  $E_z - cB_y$ , approximately representing reflected radiation, at  $y = 52\lambda_d$ . The blue dotted curve shows the initial electron temperature  $T_e = 0$  eV (blue) and the red dashed line  $T_e = 10$  eV. (b) Frequency spectrum of the outer pulse (color scale) and the ellipse representing the frequency upshift dependence (red dashed curve) as in Fig. 7(a), but for the initial electron temperature  $T_e = 10$  eV.

The energy of the outer pulse is estimated as  $\mathcal{E}_{OP} = 2.1 \times 10^{-7}$  J, or 0.53% of the source pulse. The corresponding number of photons is  $\mathcal{N}_{OP} = 6.4 \times 10^{11}$ . The reflection efficiency increases with the intensity of the driver pulse. For a driver pulse intensity of  $I_d^{PW} = 5.4 \times 10^{20}$  W/cm<sup>2</sup>, the outer pulse amplitude becomes  $1.21 \times 10^{10}$  V/m, 30.25% of the incident source pulse. The energy and number of photons increase to  $\mathcal{E}_{OP}^{PW} = 2.05 \times 10^{-6}$  J (1.02% of the source) and  $\mathcal{N}_{OP}^{PW} = 5.17 \times 10^{12}$ , respectively.

The reflectivity of the RFFOM seen in simulations requires further analytical investigation. Neglecting the forced oscillations of the mirror and correspondingly the generation of high-order harmonics, as in the model discussed in Sec. III, one can use the analytical results of Ref. [34] to calculate the reflectivity of various electron density singularities. Here the reflecting singularity consists of the cusp and two folds; the nearly flat fronts of the reflected radiation near the cusped mirror in Figs. 4(a) and 6 indicate that for such fronts the reflecting entity is a fold singularity.

## VII. THERMAL EFFECTS

In the description above, the initial electron temperature is assumed to be zero. Thermal effects on the RFM are analyzed

in Refs. [35–37]. An important factor for RFM wave breaking due to thermal effects can be mitigated by using tailored underdense plasma [38].

We note that the electron temperature in the location of an intense femtosecond laser pulse during its propagation in underdense plasma has not been measured in experiments; the estimates mentioned in the literature are based on the time-integrated observations with a typical timescale greater than 100 fs (e.g., Ref. [39]). In contrast, there are experimental measurements inconsistent with the assumption of a significant electron temperature at the location of a femtosecond laser pulse. They are represented by (i) a direct observation of a subtle structure of the wake wave by frequency-domain holography [40] and a femtosecond probe pulse [41], (ii) the measurements of the reflected spectrum and reflectivity of the RFM [9–11], and (iii) the detection of harmonics well resolved up to an order of a few hundredths from the laser self-focusing position [27,28,42] and the observation of a submicrometer pointlike sources of these harmonics [29].

In order to see how the electron temperature in the wake field modifies our scheme, we performed an additional 2D PIC simulation with an initial electron temperature of  $T_e = 10$  eV along the  $y$ -axis direction. As can be seen in Fig. 8(a), the maximum electron density corresponding to the cusp decreases by approximately 43%. The Lorentz factor of the electrons near the cusp for the initial electron temperature  $T_e = 10$  eV in Fig. 8(b) has almost the same pattern as in the case of zero initial temperature.

The outer pulse magnitude remains almost the same, as shown in Fig. 9(a), and at least the third harmonic of the upshifted base frequency can be seen. This means that the constructive interference condition for the formation of an optically coherent reflected radiation is still satisfied due to a strong localization of electrons in the cusped mirror. We note that an efficient reflection occurs also in regions where a singularity is present in the derivative of the electron density, as in the case of the wake wave breaking in thermal plasma [35,36].

## VIII. CONCLUSION

With the help of numerical simulations, we have found a physical realization of the relativistic mirror, the relativistic flying forcibly oscillating mirror. It combines the properties of the relativistic flying mirror [8] and relativistic oscillating mirror [17]. In addition, due to strong periodic modulations of the mirror surface, it acts as a reflective diffraction grating.

The RFFOM appears as a cusped mirror, the low-dimensional region of highest electron density at the joining of the electron cavity wall and the bow wave excited by the intense laser pulse (driver) propagating in plasma. It corresponds to an arrangement of universal and structurally stable density singularities, explained by catastrophe theory. The cusped mirror undergoes forced oscillations imposed by the driver pulse and moves with the group velocity of the driver. It efficiently reflects a counterpropagating relatively weak laser pulse (source). The reflected radiation spectrum exhibits well-pronounced diffractive orders and harmonic orders. These

characteristic features reveal that the cusped mirror is a relativistic flying and oscillating reflective diffraction grating. The base frequency of the reflected radiation and correspondingly all harmonic orders are strongly upshifted with respect to the base frequency of the incident source pulse, due to the double Doppler effect. In the wave number space, the harmonic orders are arranged along ellipsoids with one focus corresponding to the zero wave number.

The described scheme can be used for the generation of bright sources of high-frequency radiation. Its realization is easier than the RFM based on the reflection from the longitudinally breaking wake wave described in Refs. [8–11], where one should maintain a sufficiently slow approach to longitudinal wave breaking. While relativistic self-focusing may cause rapid longitudinal wave breaking destroying the RFM, it helps the discussed RFFOM realization.

Moreover, the described scheme provides an additional tool in laser plasma diagnostics, helping to analyze the dynamics of nonlinear physical processes in relativistic plasmas. The peculiar spectrum of the reflected radiation in the RFFOM scheme, using the head-on collision of the driver and source, substantially extends the capabilities of the scheme for probing relativistic plasma singularities by a transverse source pulse, suggested in Ref. [43]. By probing the cusped mirror by a weak counterpropagating short laser pulse, one can deduce or characterize the parameters of the laser-plasma interaction, including the geometrical properties of the first period of the wake wave (cavity and bow wave), driver pulse frequency and magnitude at the location of the cusped mirror, the velocity of the wake wave, the electron temperature or the electron

momentum distribution at the position of the cusped mirror, etc.

One of the immediate applications of such a diagnostic is control and tuning of burst intensification by singularity emitting radiation (BISER) [27–29,42], which occurs with the same parameters for the driver laser and plasma as required by the RFFOM, so that off-axis radiation from the RFFOM can be observed simultaneously with near- or on-axis BISER. In addition to the fundamental physics concerning intense laser-plasma interactions, plasma diagnostics with the described scheme may help to substantially improve the quality of the laser pulse, our main instrument, by revealing what laser parameters are the most critical. Such investigations, in the example of the laser pulse quality effects on the BISER realization, were conducted recently [44]. That work revealed some critical parameters of the laser pulse which must be improved to obtain good results and scalings predicted by theory.

#### ACKNOWLEDGMENTS

We appreciate discussions with M. Matys. The work was supported by the project High Field Initiative (Grant No. CZ.02.1.01/0.0/0.0/15\_003/0000449) from the European Regional Development Fund, and the project “IT4Innovations National Supercomputing Center LM2015070” from the Ministry of Education, Youth and Sports in Czech Republic. We acknowledge support from JSPS KAKENHI Grants No. JP16K05639 and No. JP19H00669 and Strategic Grant by the QST President: Creative Research No. 20.

- 
- [1] F. Krausz and M. Ivanov, *Rev. Mod. Phys.* **81**, 163 (2009).
  - [2] G. A. Mourou, T. Tajima, and S. V. Bulanov, *Rev. Mod. Phys.* **78**, 309 (2006).
  - [3] A. Einstein, *Ann. Phys. (Leipzig)* **322**, 891 (1905).
  - [4] K. Landecker, *Phys. Rev.* **86**, 852 (1952).
  - [5] V. I. Semanova, *Sov. Radiophys. Quantum Electron.* **10**, 599 (1967).
  - [6] R. L. Savage, Jr., C. Joshi, and W. B. Mori, *Phys. Rev. Lett.* **68**, 946 (1992).
  - [7] A. Zhidkov, T. Esirkepov, T. Fujii, K. Nemoto, J. Koga, and S. V. Bulanov, *Phys. Rev. Lett.* **103**, 215003 (2009).
  - [8] S. V. Bulanov, T. Esirkepov, and T. Tajima, *Phys. Rev. Lett.* **91**, 085001 (2003).
  - [9] M. Kando, Y. Fukuda, A. S. Pirozhkov, J. Ma, I. Daito, L. M. Chen, T. Z. Esirkepov, K. Ogura, T. Homma, Y. Hayashi, H. Kotaki, A. Sagisaka, M. Mori, J. K. Koga, H. Daido, S. V. Bulanov, T. Kimura, Y. Kato, and T. Tajima, *Phys. Rev. Lett.* **99**, 135001 (2007).
  - [10] A. S. Pirozhkov, J. Ma, M. Kando, T. Z. Esirkepov, Y. Fukuda, L.-M. Chen, I. Daito, K. Ogura, T. Homma, Y. Hayashi *et al.*, *Phys. Plasmas* **14**, 123106 (2007).
  - [11] M. Kando, A. S. Pirozhkov, K. Kawase, T. Z. Esirkepov, Y. Fukuda, H. Kiriya, H. Okada, I. Daito, T. Kameshima, Y. Hayashi *et al.*, *Phys. Rev. Lett.* **103**, 235003 (2009).
  - [12] S. V. Bulanov, T. Z. Esirkepov, M. Kando, A. S. Pirozhkov, and N. N. Rosanov, *Phys. Usp.* **56**, 429 (2013).
  - [13] M. Kando, T. Z. Esirkepov, J. K. Koga, A. S. Pirozhkov, and S. V. Bulanov, *Quantum Beam Sci.* **2**, 9 (2018).
  - [14] J. K. Koga, S. V. Bulanov, T. Z. Esirkepov, M. Kando, S. S. Bulanov, and A. S. Pirozhkov, *Plasma Phys. Contr. Fusion* **60**, 074007 (2018).
  - [15] V. V. Kulagin, V. A. Cherepenin, M. S. Hur, and H. Suk, *Phys. Plasmas* **14**, 113101 (2007).
  - [16] S. S. Bulanov, A. Maksimchuk, K. Krushelnick, K. I. Popov, V. Y. Bychenkov, and W. Rozmus, *Phys. Lett. A* **374**, 476 (2010).
  - [17] S. V. Bulanov, N. M. Naumova, and F. Pegoraro, *Phys. Plasmas* **1**, 745 (1994).
  - [18] N. M. Naumova, J. A. Nees, I. V. Sokolov, B. Hou, and G. A. Mourou, *Phys. Rev. Lett.* **92**, 063902 (2004).
  - [19] U. Teubner and P. Gibbon, *Rev. Mod. Phys.* **81**, 445 (2009).
  - [20] T. Z. Esirkepov, S. V. Bulanov, M. Kando, A. S. Pirozhkov, and A. G. Zhidkov, *Phys. Rev. Lett.* **103**, 025002 (2009).
  - [21] T. Tajima and J. M. Dawson, *Phys. Rev. Lett.* **43**, 267 (1979).
  - [22] A. Pukhov and J. Meyer-Ter-Vehn, *Appl. Phys. B* **74**, 355 (2002).
  - [23] E. Esarey, C. B. Schroeder, and W. P. Leemans, *Rev. Mod. Phys.* **81**, 1229 (2009).
  - [24] S. V. Bulanov, F. Pegoraro, A. M. Pukhov, and A. S. Sakharov, *Phys. Rev. Lett.* **78**, 4205 (1997).
  - [25] T. Z. Esirkepov, Y. Kato, and S. V. Bulanov, *Phys. Rev. Lett.* **101**, 265001 (2008).

- [26] T. Poston and I. Stewart, *Catastrophe Theory and Its Applications* (Dover, New York, 1996).
- [27] A. S. Pirozhkov, M. Kando, T. Z. Esirkepov, P. Gallegos, H. Ahmed, E. N. Ragozin, A. Y. Faenov, T. A. Pikuz, T. Kawachi, A. Sagisaka *et al.*, *Phys. Rev. Lett.* **108**, 135004 (2012).
- [28] A. S. Pirozhkov, M. Kando, T. Z. Esirkepov, P. Gallegos, H. Ahmed, E. N. Ragozin, A. Y. Faenov, T. A. Pikuz, T. Kawachi, A. Sagisaka *et al.*, *New J. Phys.* **16**, 093003 (2014).
- [29] A. S. Pirozhkov, T. Z. Esirkepov, T. A. Pikuz, A. Y. Faenov, K. Ogura, Y. Hayashi, H. Kotaki, E. N. Ragozin, D. Neely, H. Kiriya *et al.*, *Sci. Rep.* **7**, 17968 (2017).
- [30] D. F. Gordon, B. Hafizi, D. Kaganovich, and A. Ting, *Phys. Rev. Lett.* **101**, 045004 (2008).
- [31] T. D. Arber, K. Bennett, C. S. Brady, A. L. Douglas, M. G. Ramsay, N. J. Sircombe, P. Gillies, R. G. Evans, H. Schmitz, A. R. Bell *et al.*, *Plasma Phys. Contr. Fusion* **57**, 113001 (2015).
- [32] T. Esirkepov, *Comput. Phys. Commun.* **135**, 144 (2001).
- [33] P. Valenta, T. Z. Esirkepov, J. Koga, A. S. Pirozhkov, M. Kando, T. Kawachi, Y.-K. Liu, P. Fang, P. Chen, J. Mu *et al.*, *Phys. Plasmas* **27**, 032109 (2020).
- [34] A. V. Panchenko, T. Z. Esirkepov, A. S. Pirozhkov, M. Kando, F. F. Kamenets, and S. V. Bulanov, *Phys. Rev. E* **78**, 056402 (2008).
- [35] S. V. Bulanov, T. Z. Esirkepov, M. Kando, J. Koga, A. S. Pirozhkov, T. Nakamura, S. S. Bulanov, C. B. Schroeder, E. Esarey, F. Califano *et al.*, *Phys. Plasmas* **19**, 113102 (2012).
- [36] S. V. Bulanov, T. Z. Esirkepov, M. Kando, J. Koga, A. S. Pirozhkov, T. Nakamura, S. S. Bulanov, C. B. Schroeder, E. Esarey, F. Califano *et al.*, *Phys. Plasmas* **19**, 113103 (2012).
- [37] A. A. Solodov, V. M. Malkin, and N. J. Fisch, *Phys. Plasmas* **13**, 093102 (2006).
- [38] J. Mu, F. Y. Li, M. Zeng, M. Chen, Z. M. Sheng, and J. Zhang, *Appl. Phys. Lett.* **103**, 261114 (2013).
- [39] C. Zhang, C. K. Huang, K. A. Marsh, C. E. Clayton, W. B. Mori, and C. Joshi, *Sci. Adv.* **5**, eaax4545 (2019).
- [40] N. H. Matlis, S. Reed, S. S. Bulanov, V. Chvykov, G. Kalintchenko, T. Matsuoka, P. Rousseau, V. Yanovsky, A. Maksimchuk, S. Kalmykov *et al.*, *Nat. Phys.* **2**, 749 (2006).
- [41] A. Savert, S. P. D. Mangles, M. Schnell, E. Siminos, J. M. Cole, M. Leier, M. Reuter, M. B. Schwab, M. Möller, K. Poder, O. Jackel, G. G. Paulus, C. Spielmann, S. Skupin, Z. Najmudin, and M. C. Kaluza, *Phys. Rev. Lett.* **115**, 055002 (2015).
- [42] A. Sagisaka, K. Ogura, T. Z. Esirkepov, D. Neely, T. A. Pikuz *et al.*, *High Energy Density Phys.* **36**, 100751 (2020).
- [43] T. Z. Esirkepov, J. Mu, Y. Gu, T. M. Jeong, P. Valenta, O. Klimo, J. K. Koga, M. Kando, D. Neely, G. Korn, S. V. Bulanov, and A. S. Pirozhkov, *Phys. Plasmas* **27**, 052103 (2020).
- [44] A. S. Pirozhkov, T. Z. Esirkepov, T. A. Pikuz, A. Y. Faenov, A. Sagisaka *et al.*, *Quantum Beam Sci.* **2**, 7 (2018).